

This article appeared in a journal published by Elsevier. The attached copy is furnished to the author for internal non-commercial research and education use, including for instruction at the authors institution and sharing with colleagues.

Other uses, including reproduction and distribution, or selling or licensing copies, or posting to personal, institutional or third party websites are prohibited.

In most cases authors are permitted to post their version of the article (e.g. in Word or Tex form) to their personal website or institutional repository. Authors requiring further information regarding Elsevier's archiving and manuscript policies are encouraged to visit:

<http://www.elsevier.com/copyright>



Contents lists available at ScienceDirect

## Estuarine, Coastal and Shelf Science

journal homepage: [www.elsevier.com/locate/ecss](http://www.elsevier.com/locate/ecss)

## Tracking stormwater discharge plumes and water quality of the Tijuana River with multispectral aerial imagery

Jan Svejksky<sup>a,\*</sup>, Nikolay P. Nezlin<sup>b</sup>, Neomi M. Mustain<sup>a</sup>, Jamie B. Kum<sup>a</sup><sup>a</sup> Ocean Imaging Corp., 201 Lomas Santa Fe Drive, Suite 370, Solana Beach, CA 92075, USA<sup>b</sup> Southern California Coastal Water Research Project, 3535 Harbor Blvd., Suite 110, Costa Mesa, CA 92626, USA

## ARTICLE INFO

## Article history:

Received 3 March 2009

Accepted 23 January 2010

Available online 1 February 2010

## Keywords:

remote sensing

aerial surveys

river plumes

water quality

USA, California, Tijuana River

32°30'–32°35'N, 117°15'–117°05'W

## ABSTRACT

Spatial–temporal characteristics and environmental factors regulating the behavior of stormwater runoff from the Tijuana River in southern California were analyzed utilizing very high resolution aerial imagery, and time-coincident environmental and bacterial sampling data. Thirty nine multispectral aerial images with 2.1-m spatial resolution were collected after major rainstorms during 2003–2008. Utilizing differences in color reflectance characteristics, the ocean surface was classified into non-plume waters and three components of the runoff plume reflecting differences in age and suspended sediment concentrations. Tijuana River discharge rate was the primary factor regulating the size of the freshest plume component and its shorelong extensions to the north and south. Wave direction was found to affect the shorelong distribution of the shoreline-connected fresh plume components much more strongly than wind direction. Wave-driven sediment resuspension also significantly contributed to the size of the oldest plume component. Surf zone bacterial samples collected near the time of each image acquisition were used to evaluate the contamination characteristics of each plume component. The bacterial contamination of the freshest plume waters was very high (100% of surf zone samples exceeded California standards), but the oldest plume areas were heterogeneous, including both polluted and clean waters. The aerial imagery archive allowed study of river runoff characteristics on a plume component level, not previously done with coarser satellite images. Our findings suggest that high resolution imaging can quickly identify the spatial extents of the most polluted runoff but cannot be relied upon to always identify the entire polluted area. Our results also indicate that wave-driven transport is important in distributing the most contaminated plume areas along the shoreline.

© 2010 Elsevier Ltd. All rights reserved.

## 1. Introduction

Storm and dry weather runoff from coastal metropolitan areas have been increasingly recognized as a major source of marine pollution. Runoff escaping into the ocean through storm drains, rivers and creeks includes bacteria, viruses, and anthropogenic components from sewage, as well as fuel, oil, break, tire and asphalt-related compounds from roadways, and industrial and agricultural substances. Unlike sewage outfalls that release their wastewater offshore, effluent from storm drains and river mouths is released directly into the surf zone. The resultant health hazards cause temporary beach closures and possible long-term effects on coastal habitats through the accumulation of pollutants in near-shore sediments.

In southern California (SC) and other arid coastal regions, stormwater discharge is highly seasonal and episodic, and is associated with turbid plumes of polluted water emerging from river mouths after storm events. The climate of southern California is of the Mediterranean type, with distinct dry (summer) and wet (winter) seasons. The majority of annual water and sediment loads entering the ocean from land sources are linked to winter storms (Inman and Jenkins, 1999). The accumulation of pollutants on terrestrial surfaces during the dry season, which then get swept into the ocean during the first few annual storms, results in a “First Flush Effect” that has been well documented with field measurements (Bertrand-Krajewski et al., 1998; Cristina and Sansalone, 2003; Tiefenthaler and Schiff, 2003) and even from space with satellite imagery (Svejksky and Jones, 2001).

Because of the significance of the region's stormwater discharges on human health and nearshore ecosystems, the ability to better understand the spatial extents, concentration and potential pollution risk of the stormwater discharge plumes is important. High winds and rough seas following a storm often

\* Corresponding author.

E-mail address: [jan@oceani.com](mailto:jan@oceani.com) (J. Svejksky).

make ship-based field sampling of the formed plumes difficult (see [Nezlin et al., 2007](#)). Additionally, the sampling station grids that can be reasonably sampled are often not large enough to contain an entire plume and/or detailed enough to adequately resolve different characteristics within it. For this reason satellite remote sensing has been used to resolve terrestrial runoff plumes and relate their patterns to a variety of oceanic and atmospheric variables.

The most commonly used satellite data for river plume observations have included images from NOAA's Advanced Very High Resolution Radiometer (AVHRR) ([Prangsa and Roozkrans, 1989](#); [Stumpf and Goldschmidt, 1992](#); [Stumpf et al., 1993](#)), NASA's Sea-viewing Wide Field-of-view Sensor (SeaWiFS) ([Nezlin and DiGiacomo, 2005](#); [Nezlin et al., 2005](#)), and Moderate Resolution Imaging Spectrometer (MODIS) ([Miller and McKee, 2004](#); [Warrick et al., 2007](#); [Nezlin et al., 2008](#)). AVHRR, SeaWiFS and MODIS provide imagery at 1-km spatial resolution. MODIS also has channels with 250-m and 500-m resolutions that can be useful for observing river plumes. These channels provide significantly increased spatial resolution but pose problems with corrections of atmospheric attenuation which is important for any quantitative assessments. Some researchers have thus used the 250-m imagery only qualitatively from a visual standpoint ([Ahn et al., 2005](#)). Others have extended the MODIS 1-km atmospheric correction algorithm to the 500-m channels ([Shutler et al., 2007](#)) or utilized a simple clear water "dark pixel" subtraction method on a single 250-m channel ([Miller and McKee, 2004](#)). Some work has also been done using satellite sensors with higher spatial resolutions such as Landsat Thematic Mapper (30 m) ([Lira et al., 1997](#)), and SPOT (10 m) ([Ouillon et al., 1997](#)). Although the increased spatial resolution provides vastly greater structural detail within the plume signatures, the relatively low satellite revisit frequency (approximately twice per month), makes image availability after a storm event a major limitation. Imagery from these and similar sensors is also more difficult to calibrate and correct for atmospheric attenuation.

Previous post-storm studies of the SC region have utilized 1-km resolution multispectral imagery from SeaWiFS and MODIS. The studies examined satellite signatures around several major SC stormwater runoff sources and reached a number of general conclusions: the plume size estimated from the backscattering coefficient was highly correlated with the amount of rainwater precipitated over the entire watershed area and accumulated during the period preceding the plume ([Nezlin and DiGiacomo, 2005](#)); the discharges tended to be advected southward, with alongshore movement being more prevalent than across-shore transport, remained clearly distinguishable as a water mass for at least 5 days, and appeared to be primarily forced by wind stress ([Warrick et al., 2007](#)); the influence of tidal circulation on the plume area was insignificant ([Nezlin and DiGiacomo, 2005](#)). The former studies generally utilized a backscattering limit value to make a binary "plume" versus "no plume" classification for the region's waters (e.g., [Nezlin et al., 2008](#)). This approach, coupled with the relatively coarse spatial resolution of the satellite imagery (1000 m), obscured potentially important details of structure and suspended sediment load patterns within the plumes. The spatial resolution limitation also tended to blend numerous point source discharges from sources near the dominant discharge into one coherent "plume", thus distorting the spatial extents and apparent transport of the actual discharge signatures from sources targeted by the studies.

Tracking plumes from aircraft provides much higher spatial resolution than satellite imagery. A number of river plume and wastewater investigations have been done using aerial photography ([St John and Pond, 1992](#); [Ruffin, 1998](#); [da Silva et al., 2002](#)) and videography ([Webster et al., 2004](#)). Digital multispectral

imagery was also utilized by [Jorgensen and Edelvang \(2000\)](#) to map suspended sediment concentrations and aid in hydrodynamic modeling. These previous studies generally related field-collected parameters to a single image set or a very limited number of aerial images, thus limiting their observations to the discharge rate, and atmospheric and plume composition parameters existing at a particular point in time. To-date no long-term aerial imaging database has been available for examining the response of a river discharge plume to different atmospheric and oceanic conditions.

Since 2003, Ocean Imaging Corporation has been providing aerial remote sensing imagery of shoreline and offshore discharges in southern San Diego County as part of the regional water quality monitoring program. The project utilizes Ocean Imaging's multi-spectral aerial sensor which, when flown at an altitude of 3800 m provides 2.1-m spatial resolution data in 4 spectral bands. The aerial imagery was collected on a relatively regular schedule (approximately every 10 days) but additional acquisitions were also made following storm events. The imagery included the coastal region surrounding the Tijuana River (TJR) mouth – one of the most contaminated and polluting runoff sources in California ([SCCWRP, 1992](#); [DEH, 2007](#)). The archived aerial image data thus provide uniquely detailed and relatively frequent documentation of the TJR plume patterns. In addition to resolving intensity variations within the plume in great detail, the imagery also allows direct observations of other variables such as wave direction. We utilized this archive to relate the plume's distribution patterns to various oceanic and atmospheric forcing parameters at spatial resolutions not possible with satellite data. Surf zone bacterial samples available at high spatial and temporal frequency over the entire study area enabled us to examine the contamination characteristics of the runoff plume components. We thus also investigated the potential for directly using high resolution aerial imaging to establish public health risk beach closure boundaries.

## 2. The Tijuana River watershed

The TJR watershed is approximately 4465 km<sup>2</sup> in size. It straddles the United States and Mexico border, with about 72% in Mexico and 28% in the United States. More than 70% of its area is undeveloped. Near its terminus in the Pacific Ocean, the watershed's streams enter an urbanized area, mostly within the Tijuana, Mexico metropolis ([Fig. 1](#)). Within this area, 40% of the watershed's channels are unlined, while 60% constitute of concrete channels. The final 8 km are again natural, passing through the TJR Estuary and emptying into the ocean through a single opening. Four major dammed reservoirs above the urbanized region capture an estimated 70% of the watershed's runoff volume ([Englert, 1997](#)). Most of the runoff actually reaching the ocean therefore originates in the urbanized section of the watershed.

During the dry season (approximately April through September) none or only minimal flow tends to reach the TJR Estuary and no appreciable discharge thus enters the ocean. Following rain events, however, the TJR discharges excess runoff into the ocean in a highly turbid plume, readily discernible in aerial imagery. In addition to high-suspended solids concentrations, the runoff waters have been repeatedly shown to contain high levels of toxic contaminants ([Gersberg et al., 2004](#)), bacteria, and hepatitis and enteroviruses ([Gersberg et al., 2006](#)). Public health hazards posed by the TJR effluent result in beach advisory postings or downright closures for up to 4 km or more northward along the U.S. shoreline and lasting from several days to weeks. The closures are enacted by the San Diego County Department of Environmental Health (DEH) who base their decisions on exceedances of "AB 411 Standards" ([State Water Resources Control Board, 2005](#)) of indicator microorganisms in water samples collected in the surf zone.

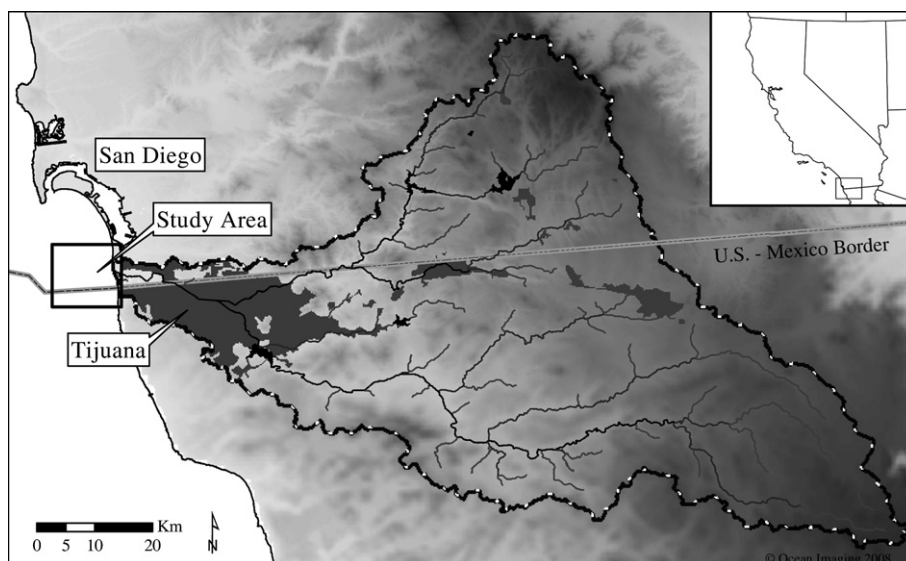


**Fig. 1.** The Tijuana River watershed with urbanized regions shaded in dark grey. (For interpretation of the references to colour in this figure legend, the reader is referred to the web version of this article.).

The frequent shoreline contamination problems associated with stormwater runoff from the TJR prompted the U.S. to construct the International Wastewater Treatment Plant (IWTP), which began operation in January, 1999. Each day the plant processes approximately 95 million liters of sewage from Tijuana's sewer system to advanced primary level and discharges it into the Pacific Ocean through an offshore outfall. The plant is connected to the TJR directly through a diverter channel system above the TJR Estuary, which diverts up to 49 million liters per day of flow from the river into the plant for treatment. The diverter system thus delays somewhat the initial entry of runoff into the estuary and the ocean following a storm, and lessens the total volume of effluent entering the ocean during the TJR active flow. Although the benefit of the IWTP on the region's shoreline contamination is a continuing point of contention, recent analysis did find some decrease in bacterial exceedances at surf zone sampling stations near the TJR mouth (Gersberg et al., 2008).

### 3. Materials and methods

#### 3.1. Aerial imagery

The multispectral imagery was acquired with a Digital Multispectral Camera (DMSC-Mk2) aerial imager manufactured by SpecTerra Ltd. in Australia. Thirty nine images were collected during rain seasons from February 2003 to February 2008. The DMSC collects 1024 by 1024 pixel image frames at 12-bit radiometric resolution with 4 separate camera channels whose imaging wavelength can be customized with narrow-band interference filters. For this analysis, a filter combination of 451/551/640/675 nm was utilized. The bandwidth for all channels was 10 nm, centered on the given wavelength. The imagery was acquired at an altitude of 3810 m, resulting in spatial resolution of 2.1 m. The system is integrated with a differential GPS/Inertial Measurement Unit, allowing automatic georeferencing of the captured image frames.

The imagery was collected along overlapping (by 40%) flight lines flown from west to east, with 60% image frame overlap. Flight times were chosen to minimize sun glint effect by imaging during 20°–35° sun angles. Most of the image acquisitions were done in

the afternoon but some were done in the morning, as is discussed further below.

Following acquisition, the image frames were merged together to form a single image. The individual frames were first corrected for vignetting effects and approximately 25% of the perimeter of each frame was discarded. The trimmed image frames were then merged together using a “feathering” routine in ERDAS image processing software. Although it was possible to radiometrically calibrate each data set with an in-flight and post-flight calibration routine utilizing a white Teflon standard target, this procedure was not performed during many of the earlier archived overflights. Therefore, an alternate calibration method had to be used to allow direct comparisons between images acquired on different days and times. A number of calibration methods have been devised and evaluated for multispectral aerial imagery. These include normalization to a spectrally flat target (Schott et al., 1988; Ben-Dor et al., 1994), empirical relationships between radiance and reflectance (Dwyer et al., 1995), and radiative transfer models. Radiative transfer models require measurements or approximations of atmospheric variables at the time of data acquisition and empirical relationships require ground reflectance measurements of targets within the imaged area, neither of which were available for the Tijuana River image data. We thus opted for the normalization approach. We utilized a grey concrete runway located at an airfield just inland of the TJR mouth as a standardization target. Concrete surfaces have been shown to represent suitable image normalization targets at visible wavelengths in previous studies (Stanz and Itten, 1982; Lawless et al., 1998). After examining the digital number (DN) values of the runway in several representative images, a 625 m<sup>2</sup> portion was used as the calibration target. An image with the target's DN values in each wavelength channel falling within the midrange of values of all other images was chosen as the normalization standard. For each image set the mean DN values of the target were then computed and the entire image was scaled to the standard values on a channel-by-channel basis. The intent was to equalize the overall intra-image brightness differences due to differences in sun angle and atmospheric conditions.

The effectiveness of the procedure was tested by recomputing the runway brightness over a larger area in each image as well as computing the average brightness of 3 differently colored flat



**Table 1**

Digital numbers (DN) for each DMSC channel used for image-to-image calibration and statistics from 39 calibrated images.

DMSC channel		451	551	640	675	551/451	640/451	675/451
Calibrated to		1400	1600	1350	1850	1.143	0.964	1.321
Runway	Average	1406	1530	1263	1850	1.090	0.915	1.300
	$\sigma$	69	67	45	66	0.058	0.030	0.036
Roof #1	Average	1246	1381	1225	1597	1.107	0.988	1.269
	$\sigma$	78	81	68	108	0.053	0.042	0.037
Roof #2	Average	1141	1172	852	1098	1.029	0.756	0.952
	$\sigma$	90	105	59	96	0.059	0.030	0.030
Roof #3	Average	1737	2019	1794	2190	1.164	1.008	1.298
	$\sigma$	126	160	123	151	0.072	0.090	0.063

building roofs along the shoreline. The statistics are shown in Table 1. They indicate that the calibration procedure was quite effective in normalizing the intra-image reflectance brightness range, allowing quantitative image-to-image DN profile comparisons.

The ocean regions of each image were then classified to separate the TJR plume from surrounding “clear” water and to differentiate the plume waters into several classes based on their spectral differences. Through experimentation, we found a threshold approach using different channel ratios to be the most effective and robust. Past analysis of the image data as well as extensive visual observations of TJR outflows during aircraft overflights indicated that the TJR plume tends to be composed of three components with distinctly different color (i.e. spectral reflectance) characteristics. The spectral contrast of each plume component was further enhanced by comparing band-to-band ratios, specifically 551/451 nm, 640/451 nm and 675/451 nm, or using the 451/551/640 nm bands as RGB components in a color image. The distinct changes in spectral reflectance were most likely due to time-dependant precipitation of specific size and material composition suspended sediment particles. The best fitting ratio thresholds for separating non-plume waters from the plume and distinguishing the three classes within the plume were determined on a subset of images and the classification procedure was then applied to the entire image data set. We classified ocean surface into four classes: “clean ocean”, “old plume” (OP), “old plume core” (OC), and “fresh plume core” (FC). The threshold values are shown in Table 2. We chose to classify the plume waters into three classes (versus less or more) because they represented the most robust ratio changes over the entire image set and coincided with visually distinct color changes in the RGB images. A final image-processing step was the application of a 300-m mask along the shoreline to mask out whitewater areas in the surf zone and exposed sand due to tidal differences.

### 3.2. Environmental data

TJR discharge data were obtained from the International Boundary Waters Commission's database in the form of daily flow rates. The daily rate was measured at a flow gauge located downstream from the IWTP diverter, immediately before the TJR enters the estuary.

Wave height and direction data were obtained for the buoy 46086 (32°29'54" N; 117°59'57" W; depth 1856.2 m) owned and maintained by National Data Buoy Center (NDBC) (<http://www.ndbc.noaa.gov>). Wind direction and velocity were also available from this sampling platform. The buoy is located offshore, 81 km due west of the TJR terminus. Our analysis of the influence of wave height on the plume size ( $E_w$ ) was based on the equation

$$E_w = W \exp(-K_w t), \quad (1)$$

where  $W$  is the wave height measured at the buoy,  $t$  is the time interval between the  $W$  measurement and the plume area size and  $K_w$  is the “forgetting factor”. According to this coefficient, the

influence of wave height decreased with time in accordance with an exponential equation with negative power coefficient. The coefficient  $K_w$  was estimated on the basis of maximum correlation between the plume size and the wave height effect  $\sum E_w$  accumulated during 10 days before the flight (the contribution of waves after a period >10 days was considered negligible). Thirty six images of 39 were used for this analysis because wave data were available only after November 2003.

Tidal fluctuation data were obtained from the NOAA “Tides and Currents” website managed by the Center for Operational Oceanographic Products and Services (CO-OPS). The tidal level was measured at hourly time intervals in San Diego (station ID: 9410170 located at 32°42'48" N, 117°10'24" W) in meters referred to Mean Lower-Low Water (MLLW) datum level. Our analysis of the influence of tidal circulation on the plume size was based on the following model. We assume that each ebb tide contributes to the plume size and this influence ( $E_t$ ) is proportional to the difference between high ( $H_h$ ) and low ( $H_l$ ) tides (“tidal prism”). The effect of each ebb tide ( $E_t$ ) decreases with time interval between the ebb tide and the observation ( $t$ , days) according to equation

$$E_t = (H_h - H_l) \exp(-K_t t) \quad (2)$$

The “forgetting factor”  $K_t$  was estimated on the basis of maximum correlation between the plume size and the accumulated tide effect  $\sum E_t$  during 10 days before the flight.

Wind speed and direction were obtained at NDBC offshore buoy 46086 and from a station within the Tijuana Estuary, maintained as part of the National Estuarine Research Reserve System ([http://cdmo.baruch.sc.edu/QueryPages/realtime.cfm?Station\\_Code=tjrtlmet](http://cdmo.baruch.sc.edu/QueryPages/realtime.cfm?Station_Code=tjrtlmet)). The station is located in the estuary 2000 m north of the TJR terminus. The wind sensor is located on a 3.5 m high aluminum tower, corresponding to 7.5 m above sea level. Prior to July 2006 hourly wind values were available from averaged measurements taken every 5 s. After that date, 15 min wind values are available. We derived hourly speed and direction from the 15 min data by averaging the preceding 4 data values for each hour.

### 3.3. Bacterial data

Shoreline bacterial sampling results were obtained from the DEH. DEH personnel collect water samples within the surf zone at

**Table 2**

Threshold band ratios used to classify imagery.

Plume class	Band ratio ( $x$ )		
	551/451	640/451	675/451
Clear ocean	$x < 0.85$	–	–
Old plume (OP)	$0.85 \leq x$	–	–
Old plume core (OC)	–	$0.45 \leq x < 0.65$	$0.55 \leq x < 0.75$
Fresh plume core (FC)	–	$0.65 \leq x$	$0.75 \leq x$

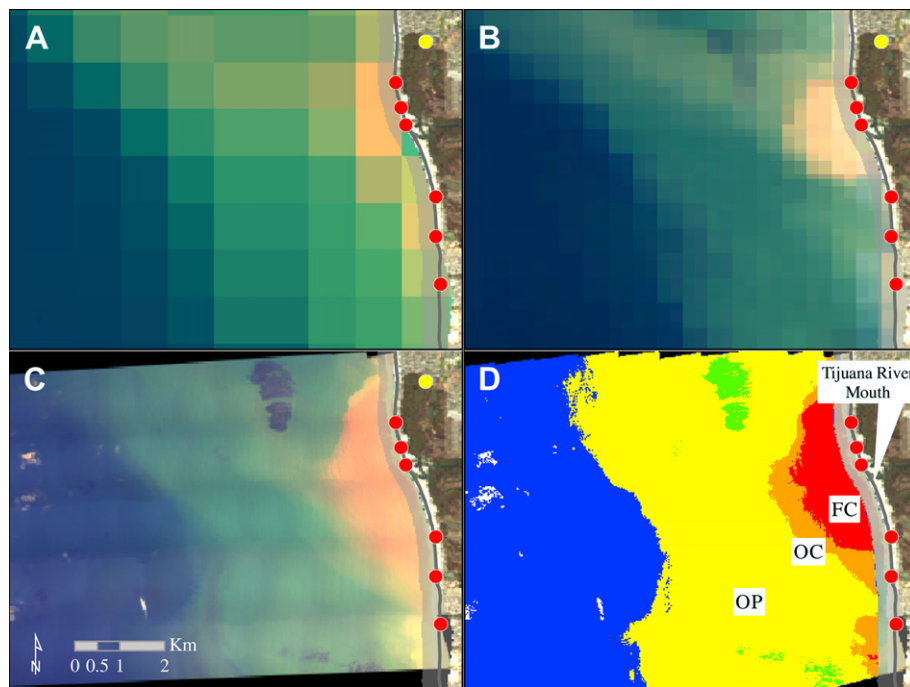


**Fig. 2.** MODIS 1-km true-color image (A) composed of bands 9 (blue), 12 (green) and 13 (red) and MODIS 500–250-m merge true-color image (B) composed of bands 4 (blue), 3 (green) and 1 (red) of the Tijuana River plume on February 24, 2005. Corresponding DMSC 2.1-m aerial image using 451/551/640-nm channels (C) and plume classification (D). Kelp growth is shown in green, DEH shoreline bacterial sampling locations are shown in red, Tijuana Estuary NERR Meteorological station location is shown in yellow. (For interpretation of the references to colour in this figure legend, the reader is referred to the web version of this article.)

established sampling locations (Fig. 2) in ankle to knee-deep water, 4–6 inches below the surface (DEH, 2007). The DEH Public Health Laboratory then utilizes the Multiple-tube Fermentation method to detect concentrations of total coliforms, fecal coliforms and enterococci. This method produces results after a 24–96-h incubation period. The DEH also utilizes the Enterolert test method for analyses of enterococci bacteria, which produces results in 24 h. As a beach closure indicator we used the California State Water Board “AB 411 Standards” (State Water Resources Control Board, 2005). The stations were classified as polluted when the FIB counts in single sample were either  $>10\,000$  “most probable number”

(MPN)/100 mL for total coliforms,  $>400$  MPN/100 mL for fecal coliforms, or  $>104$  MPN/100 mL for enterococci.

Using each bacterial sample as an indicator of microbial contamination in nearshore waters around its sampling location allowed us to evaluate the contamination characteristics of each effluent plume class in the aerial imagery. To assess the possibility of directly utilizing the classified imagery for predicting beach closure extents around the TJR mouth, we used the following accuracy assessments: total accuracy (the percentage of correctly classified stations); commission error for “polluted” and “clean” stations (the chance to erroneously include a polluted station into the clean class or a clean station into the polluted class) and omission error (the chance to miss including a polluted station in the “polluted” class or miss including a clean station in the clean class) (see details in Congalton and Green, 1999; Lillesand et al., 2004).

#### 4. Results

The 2.1-m resolution aerial imagery provides an important increase in detail over 1-km resolution MODIS or SeaWiFS satellite imagery utilized in previously published studies of runoff plumes in SC and elsewhere. Fig. 2 shows a representative example of the aerial imagery and resulting plume classifications, as well as 1-km and 250-m MODIS image data from the same day. Fig. 2A/B shows color composites of MODIS’ 1-km and 500/250-m bands. In Fig. 2B, the 500-m data were “pan sharpened” with the 250-m band in ArcGIS software. This procedure results in the most spatial detail obtainable from MODIS imagery but, as was already mentioned, is difficult to use quantitatively due to difficulties in calibration and image-to-image normalization. The two most significant sources of error in defining the plume boundaries from satellite data are the spatial integration of plume intensities into 1 km (or 500 m) pixels and the contamination of nearshore pixels by land areas partially

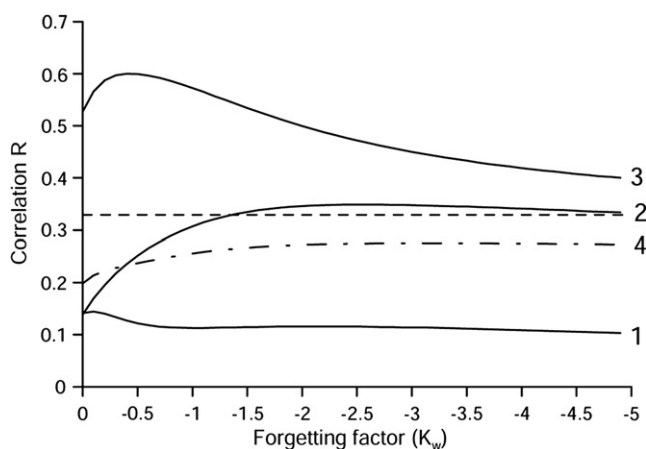


**Fig. 3.** Correlation between the size of fresh core (1), old core (2) and old plume (3) and wave height effect calculated using different “forgetting factors” ( $K_w$ ). Dashed-dot curve (4) shows the correlation between the wave height effect and the TJR discharge. Horizontal dashed line indicates the 95% confidence level of correlation coefficient at  $n = 36$ .

contained in such pixels. The spatial integration effect can erroneously increase or decrease the core plume area. The shoreline contamination effect tends to increase the apparent longshore extents of the plume signatures, makes it difficult to correctly define the plume edges and obscures potentially important intensity variations within the plume in areas closest to shore. In addition to providing significantly increased detail of the plume features, the aerial data also provide greatly increased geolocation accuracy, which is important for spatially comparing field-gathered samples to the plume features.

#### 4.1. Correlation between plume area and daily Tijuana River discharge

The TJR discharge rate (as measured on the day of the image acquisition) was the primary factor affecting the plume's size. TJR discharge explained 50–75% of the size of different parts of the plume (Table 3). Maximum correlation ( $R^2 = 0.75$ ) was observed between the discharge and the size of “fresh plume core” (FC). The FC plume component exhibits a negative linear regression intercept. This can be explained by the buffering effect of the Tijuana Estuary, which can be expected to hold and absorb a portion of the incoming runoff volume. FC discharge was observed only when the TJR discharge rate measured at the TJR entrance into the estuary exceeded  $0.30 \text{ m}^3 \text{ s}^{-1}$  (this value corresponds to 26 million liters per day). It must be noted that these rates represent runoff volume actually entering the estuary. Since the flow diverter above the estuary diverts up to 40 million liters of flow into the IWTP for processing, no flow will enter the estuary at the onset of a rain event until the upstream flow exceeds the diverter capacity. Likewise, subsequent flow into the estuary from upstream is correspondingly decreased by the diverter capacity.

The size of the older portions of the plume (OC and OP) was regulated by processes other than the TJR discharge. The inclusion of OC and OP into the total plume area decreased the correlation with TJR discharge. Adding the older plume components also caused the regression intercept to become positive (i.e. these plume components were observed even during no active TJR discharge). Under no discharge conditions, the plume area covered by the core portions (FC and OC) was  $0.35 \text{ km}^2$ ; while the area of the entire plume (including FC, OC and OP) was significantly larger ( $5.67 \text{ km}^2$ ). It thus appears that while the fresh (FC) plume component is directly linked to the TJR discharge, the older portions of the plume are enhanced by other processes such as sediment resuspension in the surf zone and perhaps by tidal ventilation from the estuary.

Including the TJR discharge measured during the day prior to image acquisition did not improve the correlation. The reason was that the correlation between discharge during the day of flight and the previous day discharge was very high ( $R^2 = 0.9915$ ).

#### 4.2. Correlation between plume area and wave height

We found no correlation between the accumulated effect of wave height ( $E_w$ ; Equation (1)) and the FC plume component (Fig. 3; curve 1). Similarly, the influence of wave height on OC was small

(Fig. 3; curve 2). The old (OP) plume component area, however, was highly correlated ( $R^2 = 0.3601$ ) with  $E_w$  (Fig. 3; curve 3). Maximum correlation corresponded to the forgetting factor  $K_w = 0.4 \text{ day}^{-1}$ . This corresponds to OP decreasing in size by a factor of 2.71 (i.e.  $\exp(1)$ ) during 2.5 days, i.e. daily decrease of the OP area was by a factor  $\sim 0.67$ . We interpret these results as indicating that a large part of the OP area resulted from wave-caused sediment resuspension, lasting a relatively short time.

Since storms are generally associated with both large waves and rainfall, it could be argued that the correlation between TJR overall plume size and wave height was fully or partially due to large river discharges occurring simultaneously with large wave conditions. To check this hypothesis, we utilized the same correlation methodology to compare wave height to TJR discharge. The correlation was small and insignificant (Fig. 3; curve 4).

#### 4.3. Correlation between plume area and tidal circulation

The correlation between tidal effect ( $E_t$ ; Equation (2)) and plume size was much lower than the effect of waves. Only for FC and OC the correlation coefficients were close to 90% confidence level (Fig. 4). The forgetting factor ( $K_t$ ) resulting in maximum correlation was  $0.3 \text{ day}^{-1}$  for FC and  $0.8 \text{ day}^{-1}$  for OC. This implies that the fresh portion of the plume was more persistent than the old portion; FC decreased in size by a factor of 2.71 during 3.33 days and OC during 1.11 days (the first value was comparable to the forgetting factor for wave height effect  $K_w$ ). The influence of tides on OC and FC was small ( $R^2$  was 0.072 and 0.059, respectively). We conclude that only 6–7% of the plume core area can be explained by tidal effects.

#### 4.4. Alongshore plume distribution

TJR plume alongshore extension was proportional to its area. The plume extended more to the south than to the north or offshore. This conclusion is based on the linear relationship (with zero intercept) between the plume area ( $S$ ) and the plume extension to the north ( $E_n$ ) and south ( $E_s$ ) using the equation  $E = A \times \sqrt{S}$  ( $S$ ), where  $A$  is a coefficient (Table 4). The coefficients characterizing the relationship between the plume area and the plume extension to the south were larger than to the north, indicating southward plume propagation. For the total plume area (FC + OC + OP) these coefficients were apparently underestimated, because the old portion of the plume extended beyond the image limits in about

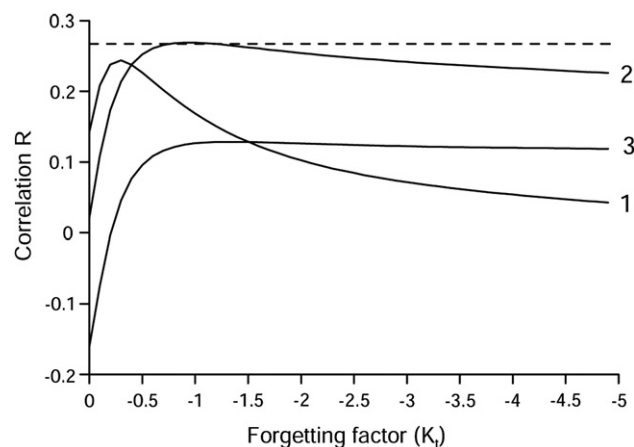


Fig. 4. Correlation between the size of fresh core (1), old core (2) and old plume (3) and tidal effect calculated using different “forgetting factors” ( $K_t$ ). Horizontal dashed line indicates the 90% confidence level of correlation coefficient at  $n = 39$ .

Table 3

Linear regression statistics between TJR discharge ( $\text{m}^3 \text{ s}^{-1}$ ) and the size ( $\text{m}^2$ ) of plume including the classes: fresh core (FC), old core (OC), and old plume (OP). All regression equations were statistically significant ( $P < 0.001$ ).

Plume classes	$R^2$	Slope	Intercept
FC	0.748	$3.70 \times 10^5$	$-1.13 \times 10^5$
FC + OC	0.586	$9.27 \times 10^5$	$+3.07 \times 10^5$
FC + OC + OP	0.503	$32.6 \times 10^5$	$+53.9 \times 10^5$

**Table 4**

Linear (with zero intercept) regression between the square function of the plume size and plume extension to the north (N) and to the south (S). Plume classes: fresh core (FC), old core (OC) and old plume (OP). Statistics: slope (A), coefficient of determination ( $R^2$ ), number of observations ( $n$ ).

Plume classes	Direction	A	$R^2$	n
FC	N	0.767	0.696	37
	S	1.220	0.856	39
FC + OC	N	0.901	0.614	39
	S	1.086	0.801	38
FC + OC + OP	N	0.920	0.794	39
	S	1.055	0.786	39
FP + OC + OP after excluding observations exceeding the image coverage	N	1.636	0.840	19
	S	1.426	0.560	18

one-half of the data sets. After exclusion of these observations, the coefficients  $A$  increased. Assuming the hypothesis that the plume tends to extend equally in all directions, we expect the plume shape to be a half-circle with radius  $E$  and area  $S$ ; as such, the coefficient  $A = \sqrt{2/\pi} = \sim 0.8$ . The observed coefficients  $A$  for northward ( $E_n$ ) plume distribution were close to this expected value. For southward plume distribution ( $E_s$ ), the observed coefficients  $A$  were higher than expected, indicating that the TJR plume tended to be retained in the nearshore zone to the south from the TJR mouth rather than propagating offshore.

To investigate a possible relationship between the plume's alongshore propagation and wave direction, we utilized wave direction measurements at the NDBC buoy 46086, averaged over 6 h prior to image acquisition. Because the buoy is located approximately 80 km offshore from the TJR mouth, it was important to verify that the directions measured at the offshore locations corresponded to subsequent wave fields affecting the TJR plume. Since many of the high resolution aerial image sets directly revealed wave signatures, we compared the image-observed wave directions with wave directions measured at the buoy. Because some images provided clearer wave signatures than others (likely related to wave height) the image-derived observations were

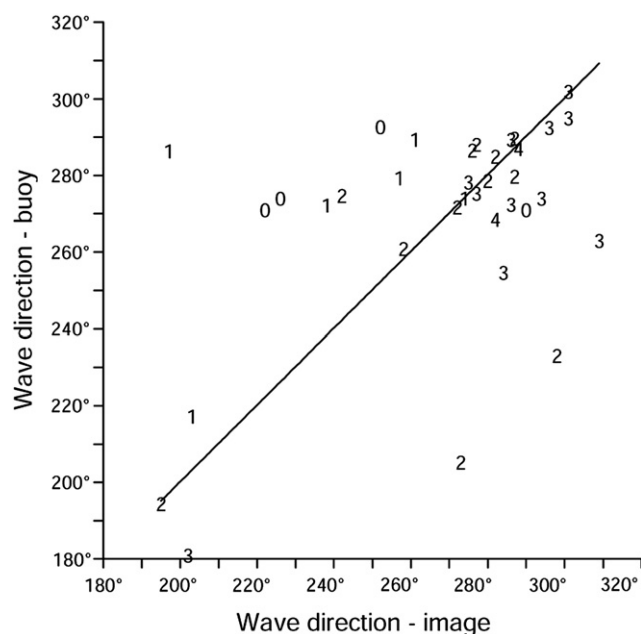


**Fig. 5.** Correlation between the wave direction measured at the offshore buoy and the wave direction estimated from the image. The numbers (0–4) indicate the quality (accuracy) of the wave direction estimated from the imagery (0–low; 4–high).

graded on a confidence of 0–4 (0 = low, 4 = high). The comparison results are shown in Fig. 5. We conclude that there is good correspondence between the 6-h mean wave direction measured at the buoy and subsequent wave direction observed directly from the imagery ( $R^2 = 0.988$ ), especially when the accuracy confidence of the direct observations was high.

Using the buoy-derived wave direction, we examined its potential effect on alongshore (i.e. north–south) distribution of the TJR plume. Because the OP area extended past the imaged area boundaries in a large number of the available images, we only addressed distribution of the plume's core components (FC and OC combined). 14 images containing FC and/or OC signatures were available for analysis. We found that the core components exhibit influence of wave direction (Fig. 6). Waves from the northwest corresponded to longer southward extensions of the plume's core areas, while waves traveling from a southwestern direction generally corresponded to the plume's core being more northward directed. Waves directed from a westerly direction (i.e. more perpendicular to the coast) corresponded to the plume's core being more evenly distributed in both directions around the river mouth. The most common wave direction affecting the TJR shoreline is between approximately 275° and 290°, i.e. from the west-northwest, corresponding to the plume's core area most commonly having a southward distribution bias.

We also examined the relationship between wind direction and the plume's core components alongshore distribution. Winds from the Tijuana Estuary station exhibit a persistent diurnal pattern: during the night they are relatively light ( $<1$  m/s) and easterly, corresponding to a “land breeze”. After sunrise, between approximately 8 and 11 local time, they reverse direction and simultaneously increase in velocity, corresponding to a characteristic daytime “sea breeze”. The winds revert back to a land breeze after sundown. The same diurnal cycle is also apparent in wind data from Lindbergh Field Airport, 19.5 km north of the estuary. The diurnal effect is not apparent, however, in wind records from the offshore buoy 46086. There is also a directional difference between winds at the shoreline stations and winds at the offshore buoy: the dominant wind direction for the 39 days with an available imagery was northwesterly at the buoy but southwesterly to westerly at the Tijuana Estuary station and at Lindbergh Field. Fig. 7 shows the relation between wind directions

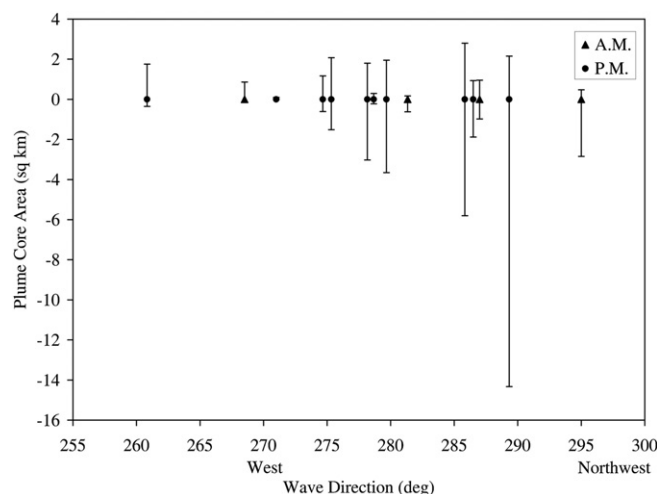


**Fig. 6.** Area of FC and OC plume components ( $\text{km}^2$ ) to the north (positive) and to the south (negative) related to wave direction measured at NDBC buoy 46086 (averaged over 6 h prior to image acquisition). AM/PM refers to time of day when the imagery was acquired.



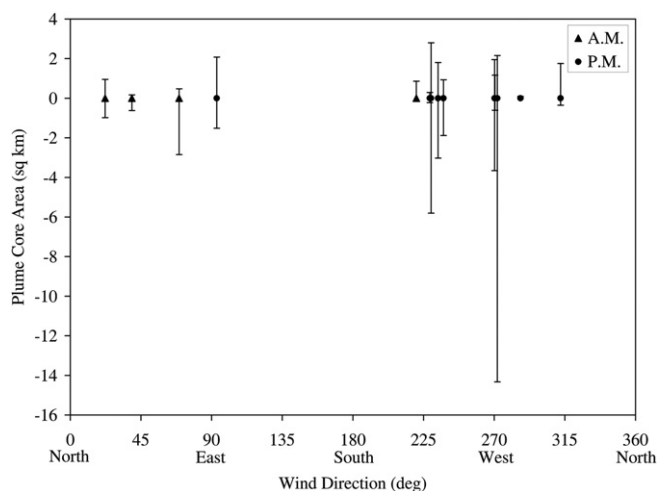


**Fig. 7.** Area of FC and OC plume components ( $\text{km}^2$ ) to the north (positive) and to the south (negative) related to wind direction measured at the Tijuana Estuary NERR (averaged over 4 h prior to image acquisition). AM/PM refers to time of day when the imagery was acquired.

and alongshore plume core distribution. The wind values represent 4 h averages prior to the time of each image. This time interval was chosen because longer time intervals for the afternoon image acquisitions would span through the diurnal direction (and velocity) shift and thus distort the true wind direction of the stronger daytime winds. Images acquired in the morning hours generally correspond to easterly winds but do not show a clear directional bias in plume direction. During the daytime sea breeze phase the plume area distribution also has no correspondence to the wind direction. The correlation results between plume distribution (as represented by percentage of total core area directed southward of the river mouth), and wave and wind direction are shown in Fig. 8. As was already noted, there is good correlation of the alongshore plume distribution with wave direction but no significant correlation with wind direction as measured by the nearby Tijuana Estuary sampling station.

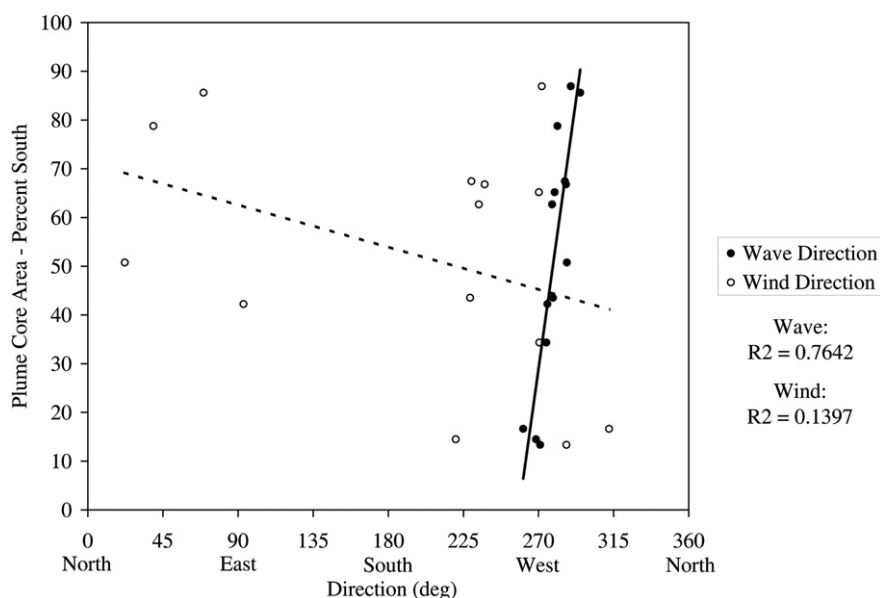


**Fig. 8.** Correlation between the alongshore plume distribution and wind and wave direction.

Fig. 9 shows two examples when the wave and wind fields existing before the image acquisition were in opposing directions. In each case the core plume components were strongly directed upcoast or downcoast corresponding to the direction of the wave field and opposite to the wind.

We also considered utilizing High-Frequency (HF) Radar surface current data from the San Diego Ocean Observing System (SDCOOS) to assess the influence of surface currents on the plume dynamics. However, the unavailability of the data in digital format as well as the generally recognized limitation of HF radar-derived current accuracies very close to shore made us forego analysis of the imaged plume patterns relative to HF radar data.

#### 4.5. TJR plume extents and shoreline bacterial pollution

The concentrations of indicator bacteria were highest in the FC plume area and gradually decreased with the age of plume components (Fig. 10). The shoreline areas encompassed in the plume core classes tended to have significantly increased bacteria concentrations, with the FC area always exceeding AB 411 standards (Table 5). The OP region showed much greater variability but tends to contain lower bacteria concentrations than the core areas, especially enterococci. Ocean waters classified as non-plume exhibited the lowest overall bacteria concentrations.

The accuracy of bacterial pollution detection using plume characteristics (Table 6) illustrates significant but loose correlation between plume optical characteristics and bacterial counts. The accuracy and error statistics were estimated on the basis of different combinations of plume classes derived from the aerial imagery (FC only, FC + OC, etc.) as “predicted” values versus shoreline bacterial sample counts as “observed” values. It is evident from these statistics, that a beach closure along the beach section in contact with the plume’s FC component would never cause an unnecessary closure (0% commission error) because all samples within FC exceed California standards. Not including other, older portions of the plume in the closure boundary, however, results in 81.5% omission of polluted sample locations and is thus inadequate in minimizing public health risk. Conversely, including the entire plume area in the closure boundary results in only 3.3% omission of polluted waters (only 3 out of 92 shoreline samples were located

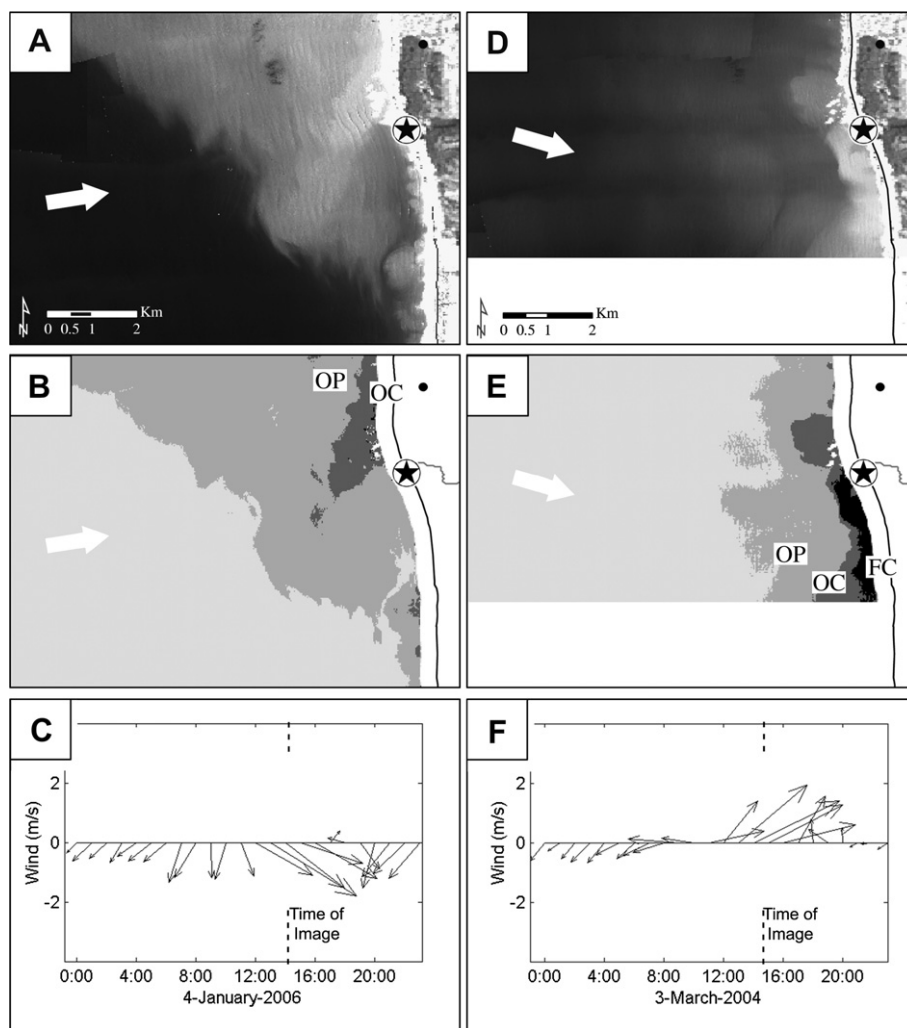


**Fig. 9.** Plume distribution, wave direction (6 h average) and hourly wind vectors on January 4, 2006 (A–C) and March 3, 2004 (D–F). Plume is shown as a grey-scale rendition of 451/551/640-nm composite image (A, D), and as classified into plume classes (B, E). Arrows at A, B, D, E indicate wave direction. Star symbol indicates TJR mouth and black dot shows location of Tijuana Estuary NERR wind measurement station. The bottom panels (D, F) show the diurnal variations of hourly wind velocity and direction, and the time of image acquisition.

outside the total plume area). This option, however, also results in 61.6% omission of unpolluted areas, i.e. a >60% overextension of necessary closure boundaries. Including only the two plume core classes to guide closure boundaries results in commission and omission errors between the two extremes.

## 5. Discussion

Different portions of the TJR plume, which we believe are related to different ages since discharge were accurately separated and mapped with the airborne imagery based on their spectral reflectance differences. Size of the most recently discharged effluent component within the TJR plume (FC) resulted directly from the TJR discharge volume, while the size of the “older” portions of the plume (OC and OP) was also regulated by factors other than the TJR freshwater flow, primarily wave resuspension. The different spectral reflectance properties of the “older” plume portions indicated lower concentrations of suspended sediment in those waters. Previous field studies of stormwater runoff plumes from rivers in southern California have shown that a large percentage of the initial suspended sediment load entering the ocean is quite rapidly precipitated out of the plume (Warrick and Milliman, 2003; Warrick et al., 2004a,b). The precipitation

process alters the particle composition and size characteristics of the plume waters as they disperse from the river outlet. The gradual precipitation in turn alters the effluent’s spectral reflectance characteristics which are apparent in our imagery. We therefore believe that the defined classes within the TJR plume reflect the relative age of each plume section. From multiple sequential flight observations we estimate the FC and OC portions represent effluent reaching the ocean within the past 12–36 h, while the effluent within the OP component is likely a combination of >2-day-old TJR discharge and sediments resuspended by surf waves.

The relationship between the plume area and the alongshore plume extension indicates that the plume tends to be retained in the nearshore zone, most commonly downcoast, rather than propagating offshore. This observation is in agreement with Warrick et al.’s (2007) observations of Southern California river plumes with satellite imagery.

Wave direction affected the shorelong distribution of the plume’s core components. The possible influence of waves on the shorelong transport of river plumes has generally not been investigated in previous studies. It is recognized that along the SC coastline waves approaching the shore from the west or northwest are likely to yield down-coast surf zone currents, while waves from the south or southwest are likely to yield up-coast surf zone

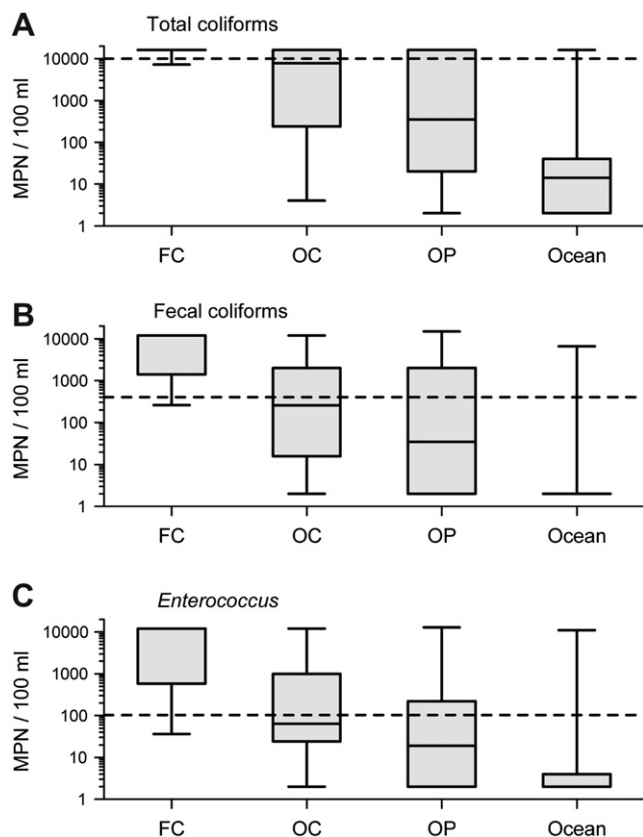


**Fig. 10.** Bacterial contamination at the surf zone sampling stations associated with the different plume classes. Box-whisker plots show medians, first and third quartiles, minima and maxima of total coliforms (A), fecal coliforms (B), and *Enterococcus* (C) in the fresh core (FC), old core (OC), old plume (OP), and ocean. Dashed lines indicate the California State Water Board "AB 411 Standards" exceedance limits.

currents (Inman and Brush, 1973; Kim et al., 2004). Studies of salinity and fecal indicator bacteria concentrations in runoff effluent from the Santa Ana River in SC indicated that contaminants tend to be transported parallel to shore by wave-driven currents (Ahn et al., 2005). This corresponds with our findings that the upcoast/downcoast distribution of the FC and OC plume components, which exhibit the highest bacteria concentrations and usually encompass the surf zone, correlate well with wave direction. In the TJR case, the wave influence is likely further enhanced by the shallow alluvial fan topography in front of the TJR mouth (Inman and Brush, 1973).

We found no correlation between wind direction and plume core alongshore distribution. This finding may appear inconsistent with earlier studies of river runoff plumes that identified wind forcing as the dominant plume-driving factor. For example, Walker et al. (2005) found the Mississippi River's plume to be very responsive to wind direction, and to reverse direction around the river delta rapidly upon the passage of wind-reversing cold fronts. Warrick et al. (2007), studied several SC river stormwater plumes and found that subsequent to the initial discharge momentum, the plumes' advection was dominated by winds. Pinones et al. (2005) linked alongshore river plume motion to wind-induced diurnal variability through salinity variations at a coastal station. These and other studies linking river plume distribution to wind forcing defined the runoff plume based on field sample grids extending out several kilometers from shore, and also utilized AVHRR, SeaWiFS or MODIS satellite imagery to visualize the plume patterns. We believe the lack of wind forcing influence in our observations is due

**Table 5**

Contingency table between the number of stations exceeding California water quality standards and the plume classes: fresh core (FC), old core (OC) and old plume (OP).

	Predicted (based on aerial imagery)				
	(1)	(2)	(3)	(4)	(5)
Observed (based on bacterial samples)	No plume	OP	OC	FC	Total
Polluted (exceeding CA standards)	3	49	23	17	92
Clean (not exceeding CA standards)	56	71	19	0	146
Total	59	120	42	17	238

to the size difference and nearshore location of the features studied. In the previous investigations "plume signatures" in the satellite imagery were identified as the total area of distinctly elevated turbidity – i.e. the entire area encompassed by FC, OC and OP classes in our aerial imagery. No effort was made to further subdivide the overall turbid region into sub-plume components. The overall plume signatures are commonly 10–50+ km in length and extend 5–10+ km offshore. Additionally, after major storms, turbidity signatures from multiple nearby point sources tend to be inseparable in the coarse resolution satellite imagery, thus enhancing the overall size of the "plume" feature. In contrast, the plume core signatures of the TJR plume in the high resolution aerial imagery that we examined with respect to wind and wave direction rarely extended offshore past 500–700 m and were anchored to the shore through the surf zone. Unlike the older (OP), more offshore-distributed plume areas, the plume core components were restricted to much shallower waters near the surf zone where wave energy can be expected to have more significant directional effects.

The diurnal cycle of winds at the river mouth versus the absence of this effect further offshore (as shown by wind fields at the NDBC buoy) should also be considered. The very light easterly winds during evening, nighttime, and early morning hours can be expected to have minimal effect on transport of the plume waters. Since we found that only 6–7% of the plume core area could be explained by tidal forcing, the dominant forces on the core plume's alongshore distribution during the land breeze hours are waves and, potentially, Coriolis accelerations which would cause an upcoast bias. This bias is not apparent in the 4 morning image acquisitions available for analysis of the plume core although, obviously, the small sample size is not sufficient to make firm conclusions about the Coriolis influence. The Tijuana Estuary station data show sea breeze conditions with increased wind speeds to span 4–6 h during the day. This contrasts markedly with wind profiles from the NDBC buoy offshore where the diurnal effects are not apparent and the wind field is usually stronger and much more persistent in speed and often in direction. Therefore, unlike the shore-anchored plume core components, the outer,

**Table 6**

Accuracy and error assessments of classification of coastal stations as "polluted" and "clean" on the basis of aerial imagery (Table 5). Plume classes: fresh core (FC), old core (OC) and old plume (OP). The statistics in row #1 (FC) were calculated assuming that only the plume class FC (column 4 in Table 5) was polluted and other classes ("No plume", OP and OC; columns 1–3 in Table 5) were clean. In row #2 (FC + OC) the plume classes FC and OC (columns 3–4 in Table 5) were considered polluted and two other classes (columns 1–2 in Table 5) were treated as clean. In row #3 (FC + OC + OP) all three plume classes (columns 2–4 in Table 5) were considered polluted and only the "No plume" class (column 1 in Table 5) was treated as clean.

Row #	Plume classes	Total accuracy (%)	Commission error (%)		Omission error (%)	
			Polluted	Clean	Polluted	Clean
1	FC	68.5	0	33.9	81.5	0
2	FC + OC	70.2	32.2	29.1	56.5	13.0
3	FC + OC + OP	60.9	50.3	5.1	3.3	61.6

older portions of the river plumes are subject to stronger and more persistent wind forcing which, as previous studies have shown, correlate well with wind direction.

The spatial detail in plume intensity and extents available from the aerial imagery is especially relevant in comparing the remotely sensed plume patterns and field-sampled bacteria concentrations. This also allows us to evaluate the possibility of utilizing high resolution aerial imagery for beach closure management, potentially in lieu of shoreline bacterial sampling. While the correlation in shoreline areas affected by the freshest effluent discharges is strong, the accuracy of predicting bacterial contamination from the imagery within the older portion of the plume is not very high. Our statistical results should be analyzed with several important considerations. First, the DEH sampled the shoreline stations approximately every 3 days, with daily sampling done at some stations on occasion. Although some of our aerial imagery was acquired on the same day as the field samples were collected, some of the data pairs available for analysis had an imaging-to-field sampling time difference of up to  $\pm 54$  h. We limited the analysis to data pairs that had a time difference of  $< 48$  h. We also discarded data pairs when a rain event occurred within its time interval, i.e. when one variable was sampled before the rain and the other after the rain impact. Nevertheless, the sample time interval inherent in a number of the data pairs can be expected to negatively affect any correlations because the TJR plume extents and/or class component distributions may have been somewhat different at the time of the bacterial sampling. Second, indicator bacteria distributions in nearshore waters have been shown to be patchy (e.g., Boehm and Weisberg, 2005; Rosenfeld et al., 2006) and subject to dilution by rip cell currents (Ahn et al., 2005). Such conditions are not expected to greatly affect the outcome of sampling within the plume's fresh areas where the effluent is greatly concentrated and sample results always exceed maximum possible measurement. In the older, more spread-out and diluted parts of the plume obscured by sediment resuspension, however, spatial heterogeneity in bacteria concentrations could affect the correlation outcomes.

The results indicate that the greatest variability and hence error contribution is found in the old (OP) portion of the plume which may be relatively unpolluted in some instances but heavily polluted in others. There are several plausible explanations for this in addition to the temporal field sampling versus image acquisition differences. As we already noted, it appears that significant portions of the OP area are the result of particle resuspension which may extend the OP area in both time and space without direct effluent input from the river itself. This could result in relatively low bacteria concentrations within the OP extents. Since the OP plume portion is the oldest, bacteria in those waters have had the longest residency time in the ocean. Their concentration is expected to decrease with time due to die-off (Davies-Colley et al., 1994), and dilution and sedimentation (Kim et al., 2004). As was already mentioned, these processes favor patchy distribution and hence higher sampling variability. There are also processes that can cause anomalous or temporary increases in bacteria concentrations and thus contribute to the high variability within the OP section. For example, small contaminated runoff sources not associated with the TJR and not identifiable in the imagery can cause localized spikes in bacteria counts within the OP extents. This is especially relevant in the Playas de Tijuana area to the south and southern Coronado shores to the north, where single sampling station exceedances sometimes occur even when there is no outflow from the TJR. Another phenomenon that appears to cause exceedance bacterial concentrations in the OP section is the aforementioned "First Flush Effect". For example, imagery acquired on October 18, 2006 after the first significant rainstorm of the season showed only minimal discharge from the TJR whose spectral characteristics

made it fall into the OP category. Shoreline samples taken on October 17–18 measured total coliform concentrations above the measurement limit at all stations up to 3400 m away from the river mouth. It cannot be ascertained if the microorganisms actually entered the ocean through the river effluent or were the result of the First Flush Effect in runoff directly from the surrounding beaches.

While previous studies in different world regions established wind forcing as the most common transport mechanism affecting the overall river plume patterns, our results show that, at least in the Tijuana River case, wave field direction is the most influential factor affecting the alongshore propagation of the freshest and most concentrated runoff effluent that pose the greatest public health hazard. This conclusion is likely applicable to other areas, as exemplified by Ahn et al.'s (2005) findings at the Santa Ana River where, during a field sampling effort, MODIS imagery showed the overall plume signature to be directed downcoast but the transport direction of fecal indicator bacteria in the surf zone was directed upcoast, in agreement with the existing wave field from the south.

The freshly discharged, most polluted plume waters can be readily identified and tracked in the aerial imagery, suggesting the possibility of utilizing such image data for setting beach closure boundaries to minimize public health risks. As was already noted, limiting the beach closures only to the FC and OC signature areas will result in few, if any, unnecessary closures. This strategy would be rarely adequate, however, since standard-exceeding indicator bacteria concentrations are very often found in the surf zone past the plume core boundaries. The alternate strategy – to close the entire beach zone impacted by FC, OC and OP signatures could, based on data available for our study, be a prudent choice if minimizing health risk is of prime importance and no other bacteriological data are available (only 3.3% of standard-exceeding samples were located outside the total plume boundary). Our analysis shows, however, that this strategy would likely result in significant (62% for the TJR data) overextension of the beach closure boundaries. Since beach closures can result in significant socioeconomic impacts for the affected regions (King, 1999) the desired strategy is to limit their extents as much as possible. The sole utilization of aerial remote sensing (or high resolution satellite imagery) for beach closure management thus carries important limitations and compromises. In areas where no field measurements are available, however, high resolution multispectral imaging could provide useful information for decreasing public health risk exposure to polluted runoff plumes.

## Acknowledgements

We thank the International Boundary Waters Commission for TJR flow rates data, the National Data Buoy Center for wind and wave data, the Center for Operational Oceanographic Products and Services for tidal level data, and Clay Clifton of the San Diego County Department of Environmental Health for bacterial pollution data. We also thank Dr. Steve Weisberg and two anonymous reviewers for their helpful comments on the manuscript. The aerial image acquisitions were co-funded by the City of San Diego, the International Boundary Waters Commission and the California State Water Resources Control Board. This study was supported by the City of San Diego Metropolitan Wastewater Department.

## References

- Ahn, J.H., Grant, S.B., Surbeck, C.Q., DiGiacomo, P.M., Nezhlin, N.P., Jiang, S., 2005. Coastal water quality impact of stormwater runoff from an urban watershed in southern California. *Environmental Science and Technology* 39, 5940–5953.
- Ben-Dor, E., Kruse, F.A., Lefkoff, A.B., Banin, A., 1994. Comparison of 3 calibration techniques for utilisation of GER 63-channel aircraft scanner data of Makhtesh-



- Ramon, Negev, Israel. Photogrammetric Engineering and Remote Sensing 60, 1339–1354.
- Bertrand-Krajewski, J.-L., Chebbo, G., Saget, A., 1998. Distribution of pollutant mass vs volume in stormwater discharges and the first flush phenomenon. *Water Research* 32, 2341–2356.
- Boehm, A.B., Weisberg, S.B., 2005. Tidal forcing of enterococci at marine recreational beaches at fortnightly and semidiurnal frequencies. *Environmental Science and Technology* 39, 5575–5583.
- Congalton, R.G., Green, K., 1999. Assessing the Accuracy of Remotely Sensed Data: Principles and Practices. Lewis Publishers, Boca Raton, p. 137.
- Cristina, C.M., Sansalone, J.J., 2003. First flush, power law and particle separation diagrams for urban storm-water suspended particulates. *Journal of Environmental Engineering-ASCE* 129, 298–307.
- Davies-Colley, R.J., Bell, R.G., Donnison, A.M., 1994. Sunlight inactivation of enterococci and fecal coliforms in sewage effluent diluted in seawater. *Applied and Environmental Microbiology* 60, 2049–2058.
- da Silva, J.F., Duck, R.W., Hopkins, T.S., Anderson, J.M., 2002. Nearshore circulation revealed by wastewater discharge from a submarine outfall, Aveiro Coast, Portugal. *Hydrology and Earth System Sciences* 6, 983–988.
- DEH, 2007. San Diego County 2006 Beach Closure and Advisory Report. County of San Diego Department of Environmental Health, Land and Water Quality Division, San Diego, 25 pp., available online at: [http://www.co.san-diego.ca.us/deh/water/docs/bb\\_2006\\_bcr\\_summary.pdf](http://www.co.san-diego.ca.us/deh/water/docs/bb_2006_bcr_summary.pdf).
- Dwyer, J.L., Kruse, F.A., Lefkoff, A.B., 1995. Effects of empirical versus model based reflectance calibration on automated analysis of imaging spectrometer data: a case study from Drum Mountains, Utah. *Photogrammetric Engineering and Remote Sensing* 61, 1247–1254.
- Englert, P.F., 1997. Characterizing Urban Storm Pollution in the Tijuana River Watershed. San Diego State University, 206 pp.
- Gersberg, R., Tiedge, J., Gottstein, D., Altmann, S., Watanabe, K., Luderitz, V., 2008. Effect of the South Bay Ocean Outfall (SBOO) on ocean beach water quality near the USA-Mexico border. *International Journal of Environmental Health Research* 18, 149–158.
- Gersberg, R.M., Daft, D., Yorkey, D., 2004. Temporal pattern of toxicity in runoff from the Tijuana River Watershed. *Water Research* 38, 559–568.
- Gersberg, R.M., Rose, M.A., Robles-Sikisaka, R., Dhar, A.K., 2006. Quantitative detection of hepatitis A virus and enteroviruses near the United States-Mexico border and correlation with levels of fecal indicator bacteria. *Applied and Environmental Microbiology* 72, 7438–7444.
- Inman, D.L., Brush, B.M., 1973. Coastal challenge. *Science* 181, 20–32.
- Inman, D.L., Jenkins, S.A., 1999. Climate change and the episodicity of sediment flux of small California rivers. *Journal of Geology* 107, 251–270.
- Jorgensen, P.V., Edlevang, K., 2000. CASI data utilized for mapping suspended matter concentrations in sediment plumes and verification of 2-D hydrodynamic modelling. *International Journal of Remote Sensing* 21, 2247–2258.
- Kim, J.H., Grant, S.B., McGee, C.D., Sanders, B.F., Largier, J.L., 2004. Locating sources of surf zone pollution: a mass budget analysis of fecal indicator bacteria at Huntington Beach, California. *Environmental Science and Technology* 38, 2626–2636.
- King, P., 1999. The Fiscal Impact of Beaches in Southern California. Final Report for California Department of Boating and Waterways. Public Research Institute, San Francisco State University, San Francisco, 29 pp., available online at <http://sccoos.ucsd.edu/docs/PhilipKing.pdf>.
- Lawless, K.P., Milton, E.J., Anger, C.O., 1998. Investigation of changes in the reflectance of ground calibration targets (asphalt and concrete), information for sustainability. In: 27th International Symposium on Remote Sensing of Environment, ERIM, Ann Arbor, Michigan, pp. 597–600.
- Lillesand, T.M., Kiefer, R.W., Chipman, J.W., 2004. Remote Sensing and Image Interpretation, fifth ed. John Wiley & Sons, New York, 763 pp.
- Lira, J., Morales, A., Zamora, F., 1997. Study of sediment distribution in the area of the Panuco river plume by means of remote sensing. *International Journal of Remote Sensing* 18, 171–182.
- Miller, R.L., McKee, B.A., 2004. Using MODIS Terra 250 m imagery to map concentrations of total suspended matter in coastal waters. *Remote Sensing of Environment* 93, 259–266.
- Nezlin, N.P., DiGiacomo, P.M., 2005. Satellite ocean color observations of stormwater runoff plumes along the San Pedro Shelf (southern California) during 1997–2003. *Continental Shelf Research* 25, 1692–1711.
- Nezlin, N.P., Weisberg, S.B., Diehl, D.W., 2007. Relative availability of satellite imagery and ship-based sampling for assessment of stormwater runoff plumes in coastal southern California. *Estuarine, Coastal and Shelf Science* 71, 250–258.
- Nezlin, N.P., DiGiacomo, P.M., Stein, E.D., Ackerman, D., 2005. Stormwater runoff plumes observed by SeaWiFS radiometer in the Southern California Bight. *Remote Sensing of Environment* 98, 494–510.
- Nezlin, N.P., DiGiacomo, P.M., Diehl, D.W., Jones, B.H., Johnson, S.C., Mengel, M.J., Reifel, K.M., Warrick, J.A., Wang, M., 2008. Stormwater plume detection by MODIS imagery in the southern California coastal ocean. *Estuarine, Coastal and Shelf Science* 80, 141–152.
- Quillon, S., Forget, P., Froidefond, J.-M., Naudin, J.-J., 1997. Estimating suspended matter concentrations from SPOT data and from field measurements in the Rhone river plume. *Marine Technology Society Journal* 31, 15–20.
- Pinones, A., Valle-Levinson, A., Narvaez, D.A., Vargas, C.A., Navarrete, S.A., Yuras, G., Castilla, J.C., 2005. Wind-induced diurnal variability in river plume motion. *Estuarine, Coastal and Shelf Science* 65, 513–525.
- Prangmsma, G.J., Roozekrans, J.N., 1989. Using NOAA AVHRR imagery in assessing water-quality parameters. *International Journal of Remote Sensing* 10, 811–818.
- Rosenfeld, L.K., McGee, C.D., Robertson, G.L., Noble, M.A., Jones, B.H., 2006. Temporal and spatial variability of fecal indicator bacteria in the surf zone off Huntington Beach, CA. *Marine Environmental Research* 61, 471–493.
- Ruffin, K.K., 1998. The persistence of anthropogenic turbidity plumes in a shallow water estuary. *Estuarine, Coastal and Shelf Science* 47, 579–592.
- SCCWRP, 1992. Surface runoff to the southern California Bight. In: Cross, J.N., Francisco, C. (Eds.), SCCWRP Annual Report 1990–1991 and 1991–1992. Southern California Coastal Water Research Project Authority, Long Beach, pp. 19–28.
- Schott, J.R., Salvaggio, C., Volchok, W.J., 1988. Radiometric scene normalization using pseudoinvariant features. *Remote Sensing of Environment* 26, 1–16.
- Shutler, J.D., Land, P.E., Smyth, T.J., Groom, S.B., 2007. Extending the MODIS 1 km ocean colour atmospheric correction to the MODIS 500 m bands and 500 m chlorophyll-*a* estimation towards coastal and estuarine monitoring. *Remote Sensing of Environment* 107, 521–532.
- St John, M.A., Pond, S., 1992. Tidal plume generation around a promontory: effects on nutrient concentration and primary productivity. *Continental Shelf Research* 12, 339–354.
- Stanz, K., Itten, K.I., 1982. Reflective properties of asphalt and concrete surfaces. In: International Symposium of the ISPRS, vol. WG-VII. Toulouse, France, pp. 307–316.
- State Water Resources Control Board, 2005. California Ocean Plan, 57 pp.
- Stumpf, R.P., Goldschmidt, P.M., 1992. Remote sensing of suspended sediment discharge into the western Gulf of Maine during the April 1987 100-year flood. *Journal of Coastal Research* 8, 218–225.
- Stumpf, R.P., Gelfenbaum, G., Pennock, J.R., 1993. Wind and tidal forcing of a buoyant plume, Mobile Bay, Alabama. *Continental Shelf Research* 13, 1281–1301.
- Svejksky, J., Jones, B.H., 2001. Satellite imagery detects coastal stormwater and sewage runoff. *Eos* 82, 621–630.
- Tiefenthaler, L.L., Schiff, K.C., 2003. Effects of rainfall intensity and duration on first flush of stormwater pollutants. In: Weisberg, S.B., Elmore, D. (Eds.), Southern California Coastal Water Research Project Annual Report 2001–2002. Southern California Coastal Water Research Project Authority, Westminster, CA, pp. 209–215.
- Walker, N.D., Wiseman Jr., W.J., Rouse Jr., L.J., Babin, A., 2005. Effects of river discharge, wind stress, and slope eddies on circulation and the satellite-observed structure of the Mississippi River plume. *Journal of Coastal Research* 21, 1228–1244.
- Warrick, J.A., Milliman, J.D., 2003. Hyperpynal sediment discharge from semiarid southern California rivers: implications for coastal sediment budgets. *Geology* 31, 781–784.
- Warrick, J.A., Mertes, L.A.K., Washburn, L., Siegel, D.A., 2004a. Dispersal forcing of southern California river plumes, based on field and remote sensing observations. *Geo-Marine Letters* 24, 46–52.
- Warrick, J.A., Mertes, L.A.K., Washburn, L., Siegel, D.A., 2004b. A conceptual model for river water and sediment dispersal in the Santa Barbara Channel, California. *Continental Shelf Research* 24, 2029–2043.
- Warrick, J.A., DiGiacomo, P.M., Weisberg, S.B., Nezlin, N.P., Mengel, M.J., Jones, B.H., Ohlmann, J.C., Washburn, L., Terrill, E.J., Farnsworth, K.L., 2007. River plume patterns and dynamics within the Southern California Bight. *Continental Shelf Research* 27, 2427–2448.
- Webster, C.F., Fleischer, R.S., Everitt, J.H., Davis, M.R., Escobar, E., Repic, R.L., 2004. Assessing a wastewater discharge to the subtropical Rio Grande using aerial videography and in situ physicochemistry. *Geocarto International* 19, 41–48.